Comparative Analysis of Positivity Probing: Diphoton Channel at CEPC vs. Photon-Fusion Processes at LHC

Chi Shu
cshu20@fudan.edu.cn

Current work with Prof. Jiayin Gu

Introduction

Certain dim-8 operators are subject to the so-called positivity bounds, assuming the underlying UV physics is consistent with the fundamental principles of quantum field theory, including unitarity, locality, analyticity and Lorentz invariance. Prior studies have identified constraints on dim-8 operators through the diphoton channel, particularly at CEPC. In this study, we probe into the exclusive photon-fusion processes at the LHC to extract constraints on dim-8 operators.

CEPC
Diphoton Channel

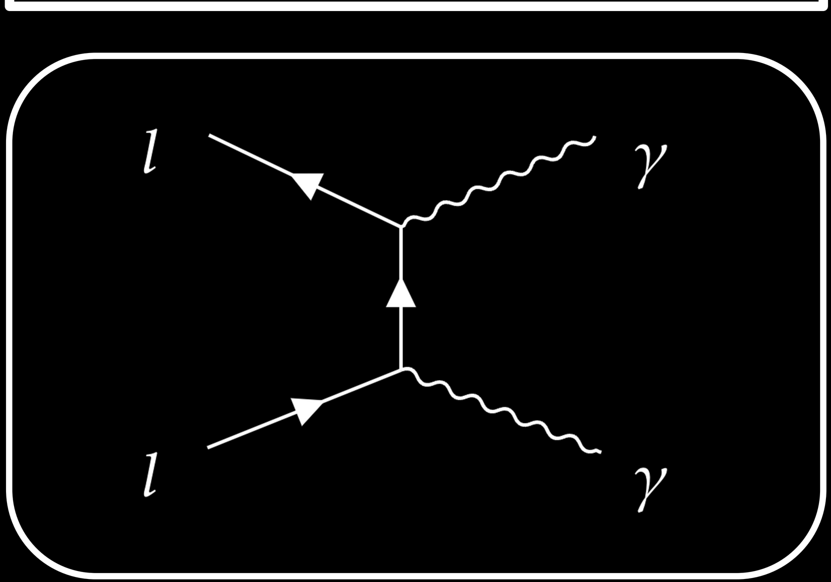

$$\frac{d\sigma\,(\gamma\gamma\to\ell^+\ell^-)}{d|\cos\theta|} = \frac{e^4}{8\pi s}\left[\frac{1+c_\theta^2}{1-c_\theta^2} + (a_L+a_R)\,\frac{s^2\,(1+c_\theta^2)}{8e^2v^4}\right]$$

LHC
Photon Fusion process

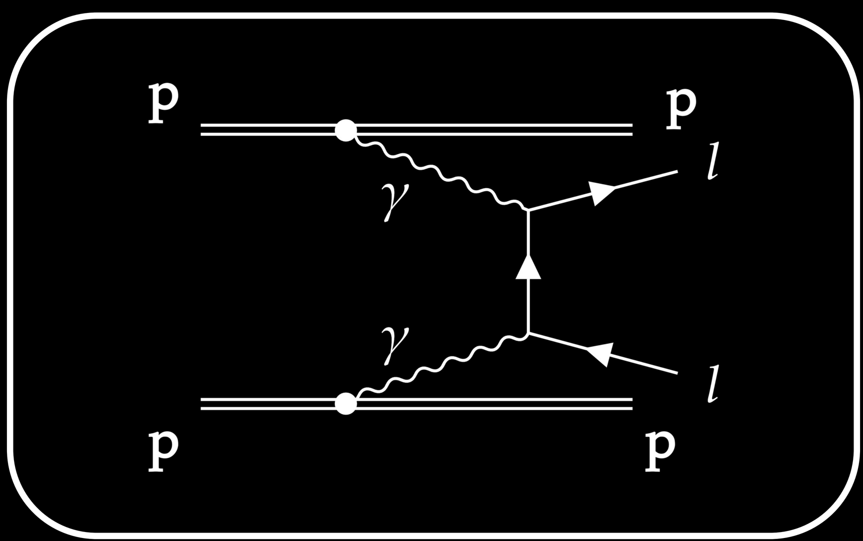

$$\frac{d\sigma\,(AB\to A\,(\gamma\gamma\to l^+l^-)\,B)}{d|\cos\theta|} = \int \frac{dE_{\gamma_1}}{E_{\gamma_1}}\frac{dE_{\gamma_2}}{E_{\gamma_2}}\frac{d^2N^{(AB)}_{\gamma_1/Z_1,\gamma_2/Z_2}}{dE_{\gamma_1}\,dE_{\gamma_2}}\frac{d\sigma\,(\gamma\gamma\to l^+l^-)}{d|\cos\theta|}$$

The parameters a_L and a_R are dim-8 operators in EFT. The positivity bounds, derived from QFT principles, are

$$a_L, a_R > 0,$$

which implies cross sections are slightly larger than the SM case.
In LHC scenario, we use the photon PDF provided by Ref. [1].

Comparison Analysis

For the HL-LHC pp run of 3 ab^{-1}, we perform a binned analysis, with $m_{ll} \in [100,1500]$ GeV and a bin width of 50 GeV. The analysis on lepton colliders is reproduced from Ref. [2]. We take 240 GeV runs of CEPC and FCC-ee with luminosity 20 ab^{-1} and 5 ab^{-1} respectively, and 250 GeV run of ILC with luminosity 0.9 ab^{-1} and polarization of $(\pm 0.8, \mp 0.3)$.

This figure shows the constraint on measurements of a_L and a_R. The grey area is forbidden by positivity bounds.

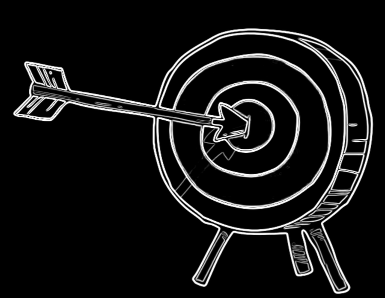

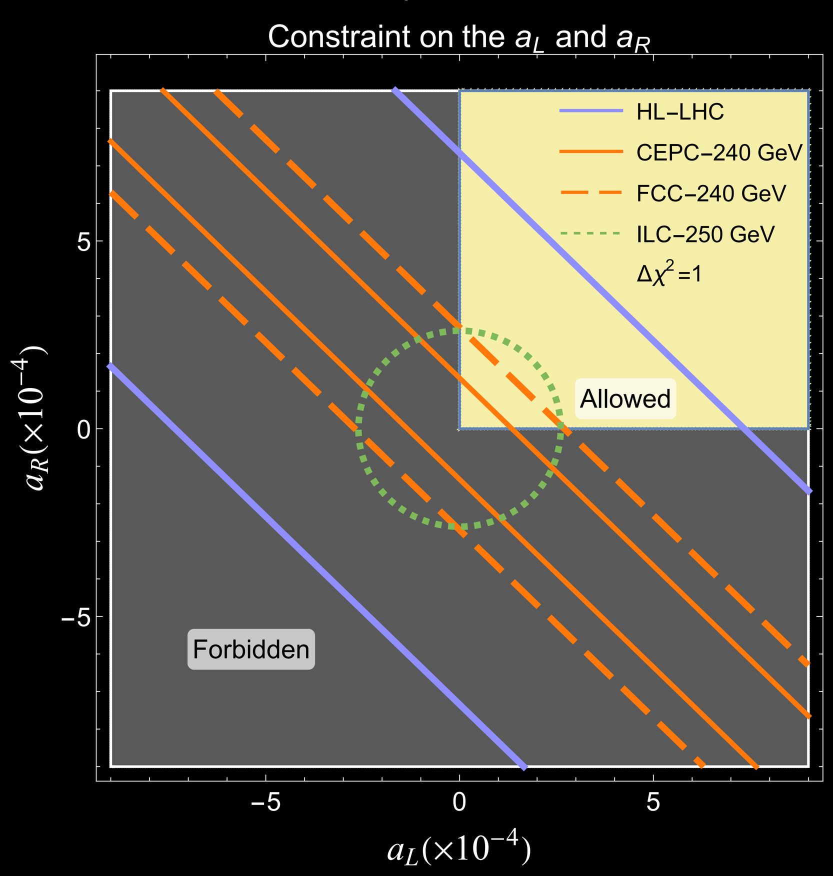

EFT Validity Test

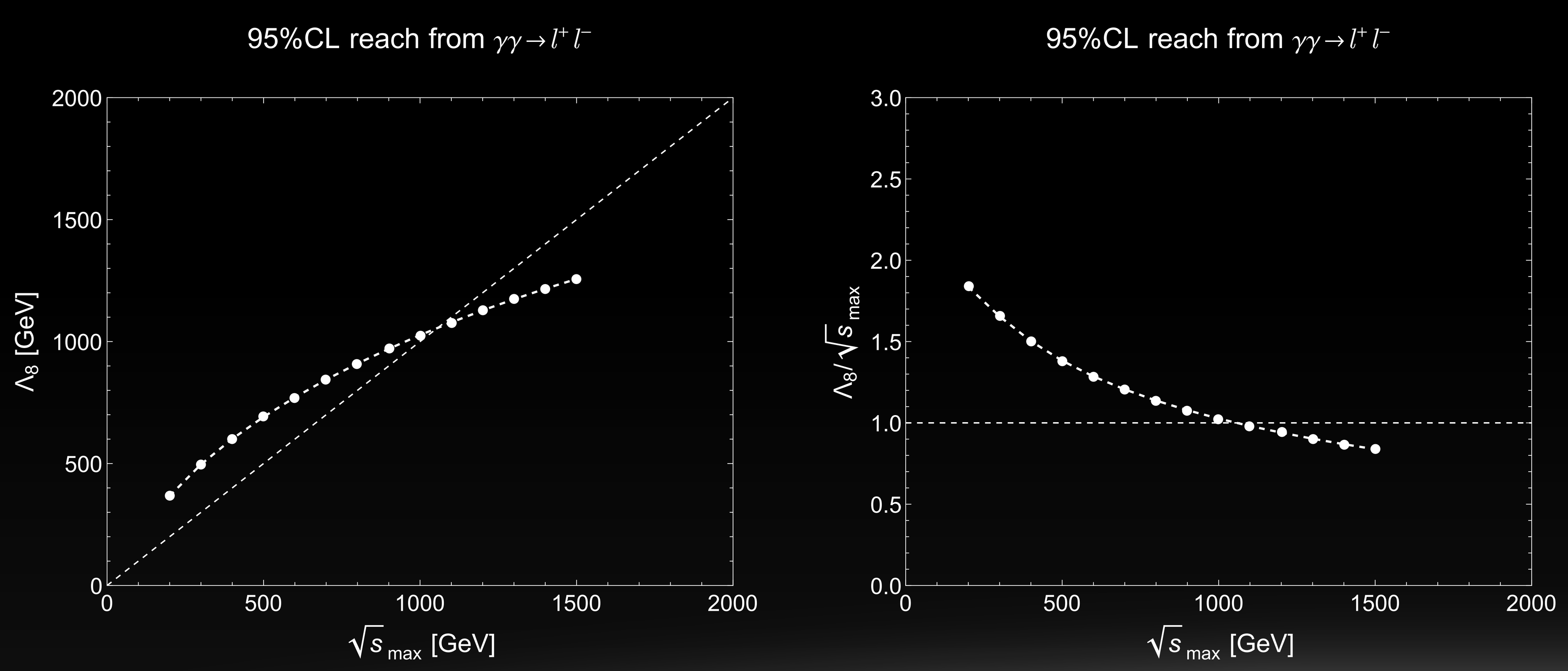

$\gamma q \to \gamma q$ processes

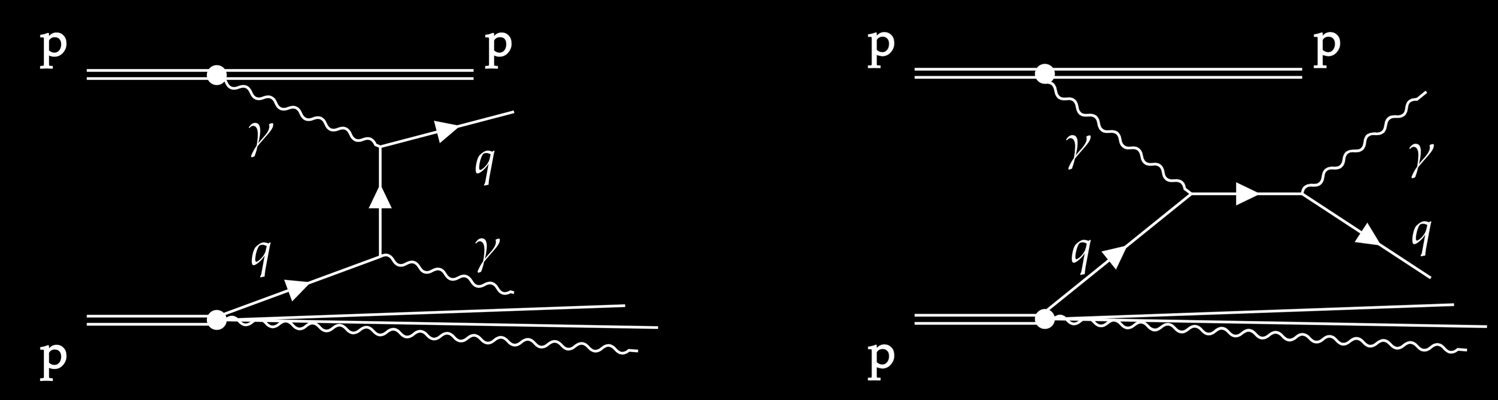

Here, we propose $\gamma q \to \gamma q$ can also be measured and is sensitive to a set of dim-8 operators involving quarks, which are subject to positivity bounds as well.

$$\frac{d\sigma\,(\gamma q\to\gamma q)}{d|\cos\theta|} = \frac{Q^4e^4}{4\pi s}\left[\frac{2}{1-c_\theta^2} - (a_L+a_R)\,\frac{s^2}{2Q^2e^2v^4}\right]$$

This process has two advantages: first, the final state photon could be used to reduce QCD backgrounds; second, the initial state quark has a larger PDF than photon, so the cross section of this process is larger, especially at high energies. We then convolute it with the photon PDF and the quark PDF, from MMHT PDF[3].

The reach is significantly better, with precision of $\sim 10^{-5}$ for $a_L + a_R$ (assuming the operator coefficients are universal for all quark flavors) and a reach on Λ_8 of about $2 \sim 4$ TeV. With b-tagging, one is also able to pick out and probe the b-quark related operators with a reasonable sensitivity.

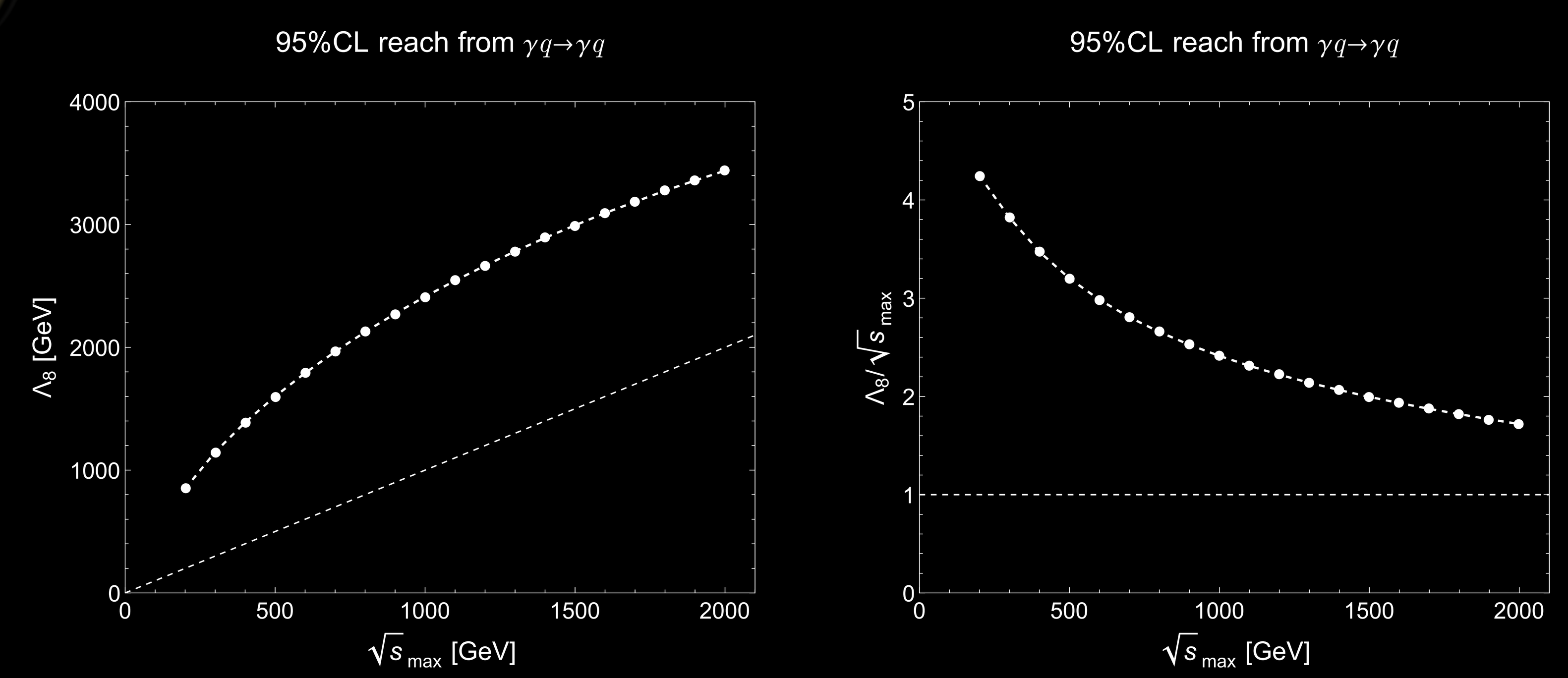

Conclusion

Our analysis reveals that for dim-8 operators involved in diphoton and dilepton, the CEPC holds potential advantages over the LHC, reaching more precise results. While LHC has advantages in $\gamma q \to \gamma q$ processes, a sufficiently large ratio ($\gtrsim 2$) between the new physic scale that can be reached (assuming order one couplings) and the maximum final-state center-of-mass energy can be achieved.

Reference:
[1] JHEP. 09 (2022) 248, H.-S. Shao and D. d'Enterria.
[2] Phys. Rev. Lett. 129 (2022), no. 1 011805, Jiayin Gu, Lian-Tao Wang and Cen Zhang.
[3] Eur Phys J C 75 (2015), no. 5 204, L. A. Harland-Lang, A. Martin, P. Motylinski, and R. Thorne

Jet Clustering performance based on Quantum Approximate Optimization Algorithm (QAOA)

Dong Liu (THU), Yunheng Ma (BAQIS), Chen Qian (BAQIS),
Manqi Ruan (IHEP), Weifeng Zhuang (BAQIS), Yongfeng Zhu (PKU), Chen Zhou (PKU)

Motivation:

- Finding useful applications for near-term quantum machines is interesting in the quantum era.
- Quantum Approximate Optimization Algorithm (QAOA) has a high potential to showcase the advantages of quantum computing in the NISQ era.
- Jet clustering, which is actually a combinatorial problem, can be explored with QAOA after mapping a collision event into a graph.

Introduction:

MaxCut:

- Graph : Set of vertices or nodes connected by weighted edges (W_{ij})
- cut : Partition of vertices into two disjoint subsets
- Goal : Letting the weighted sum of edges with two nodes located in two subsets as large as possible

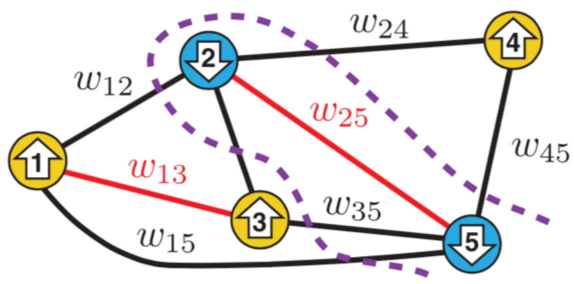

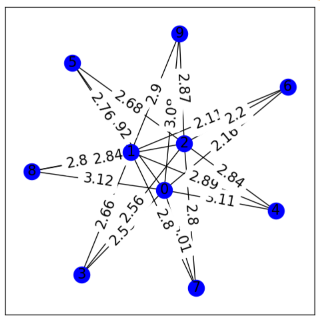

QAOA for MaxCut:

1. Define problem Hamiltonian $\hat{H}_C = \frac{1}{2}\sum_{(i,j)\in E} w_{ij}(I - Z_i Z_j)$, and mixer Hamiltonian $\hat{H}_M = \sum_{j\in V} X_j$
2. Initialize the quantum circuit in the highest energy state of the mixer Hamiltonian $|s\rangle = |+\rangle^{\otimes n} = \frac{1}{\sqrt{2^n}}\sum_{x\in(0,1)^n} |x\rangle$,
3. Define the unitaries, $\hat{U}_C(\gamma) = e^{-i\gamma\hat{H}_C}$ and $\hat{U}_M(\beta) = e^{-i\beta\hat{H}_M}$, where γ and β are variational parameters of the circuit.
4. Initialize the 2P variational parameters and the final state output by the circuit $|\psi_P(\gamma,\beta)\rangle = \prod_{j=1}^{P} U(\beta_j, \hat{H}_M)U(\gamma_j, \hat{H}_C)|s\rangle$.
5. By repeated measurements, the expectation value of the $\hat{H}_C$ with respect to the $|\psi_P(\gamma,\beta)\rangle$ is $F_P(\gamma,\beta) = \langle\psi(\gamma,\beta)|\hat{H}_C|\psi_P(\gamma,\beta)\rangle$
6. The variational parameters are optimized by a classical optimizer $(\gamma^*,\beta^*) = \arg\max_{\gamma,\beta} F_P(\gamma,\beta)$, and the approximation ratio α is defined as $\alpha = \frac{F_P(\gamma^*,\beta^*)}{C_{max}}$, where C_{max} corresponds to the best value of $F_P(\gamma,\beta)$

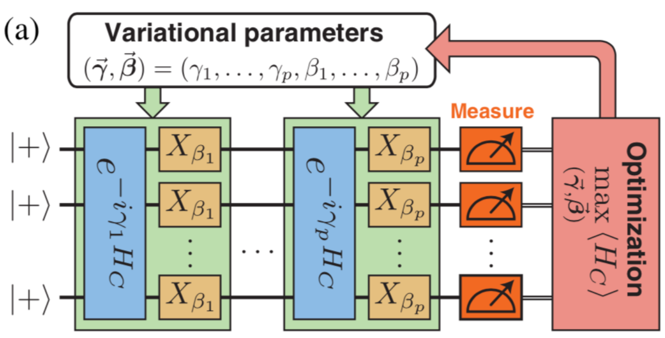

Mapping a collision event into a graph:

- The particles are represented with nodes and the weight of the edge is calculated as the angle between two particles.
- For an event with n particles, each particle can have edges with other n-1 particles, but we only keep the k edges with the largest weight.
- A graph with nodes=10 and k = 3.

Performance analysis:

- **The dependence of QAOA performance** on the value of k, depth, and nodes within the graph. GW is a classical algorithm used to solve MaxCut.

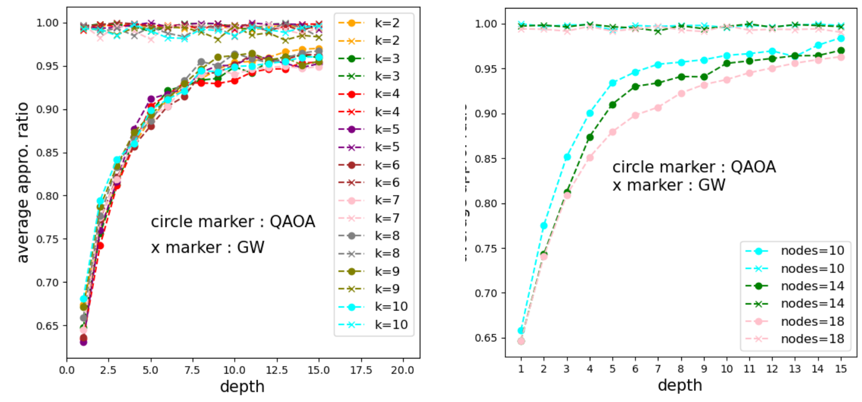

- **Parameter transferability:** The hard problem of the QAOA is variational parameters optimization. Abstract optimized parameters from 100 graphs, and reuse these optimized parameters to similar graphs to sample directly, which can conserve computing resources with a performance decrease of less than 2% compared to regular optimization procedure, as initial parameters to optimize in a further step, which can improve the QAOA performance. The further optimized parameters are more concentrated, which illustrates the parameter transferability in another aspect. The success rate is defined as the ratio of graphs with an approximation ratio larger than 0.96.

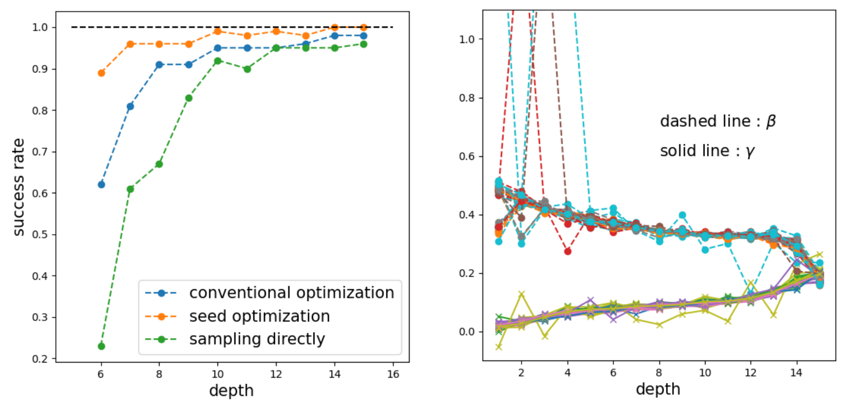

- **Jet clustering performance** can be evaluated with the angle between the reconstructed jet and the corresponding quark.

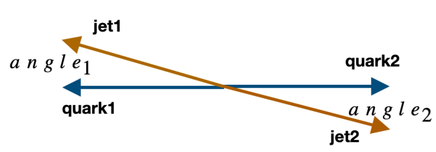

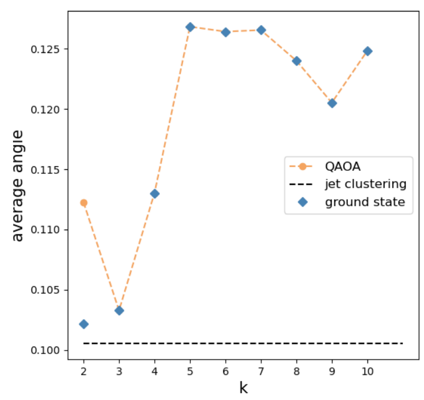

Summary:

- Based on the jet clustering problem, the QAOA performance would be better with increasing depth of circuit, and worse with increasing number of nodes within the graph, independent of the graph's connectivity.
- The optimized parameters can be reused on similar graphs to sample directly with a performance decrease of less than 2% but conserve computing resources. When seeing optimized parameters as initial parameters and optimizing in a further step, the QAOA performance would be better.
- A well-modeling method and quantum algorithm are needed for jet clustering in the quantum era.

New Physics Investigations with Triangular Singularity

Yugen Lin[1]

[1]Institute of High Energy Physics, Chinese Academy of Sciences E-mail: linyugen@ihep.ac.cn

Introduction

Loop-induced processes involving new physics particles can readily satisfy Landau Equation and trigger triangular singularities at high energy colliders, leading to fully visible Standard Model final states. Four-particle vertices in new physics allow triangular singularity diagrams to evade large virtuality suppression. We discuss several typical scenarios in supersymmetric models, and three types of final-state kinematic features at the collider. We identify an ‘everything on shell’ triangular singularity diagram only involving bosonic couplings, which has the potential to completely avoid large virtuality suppression. Such a virtuality-free diagram is missing in the Standard Model at the electroweak scale, and it becomes available in new physics models.

Triangle Singularity (TS)

Triangle Singularity, the kinematic situation when all three intermediate particles in a triangle loop diagram for a $1 \to 2$ process become on-shell. Triggering TS requires the internal momenta k_i^μ in a triangle diagram to satisfy the Landau Equation,

$$\sum_i \alpha_i k_i^\mu = 0 \text{ and } k_i^2 - m_i^2 = 0, \quad (i = 1, 2, 3), \tag{1}$$

where $\sum_i \alpha_i = 1$ and $0 < \alpha_i < 1$ should be satisfied at leading Landau singularity. These conditions can be equivalently expressed in relation with the external invariant momenta p_k^2 that connect to k_i, k_j,

$$\beta_i + \sum_j^{j \neq i} \beta_j y_{ij} = 0, \quad y_{ij} \equiv \frac{m_i^2 + m_j^2 - p_k^2}{2 m_i m_j}, \tag{2}$$

in which $i \neq j \neq k$ and $\beta_i \equiv \alpha_i m_i$. TS typically describes a heavy state splitting into lighter states with three internal on-shell particles with various masses. The corresponding classical processes are described below. Consider the rest frame of particle C. Particle C first decays into particles 1 and 2 flying back to back, then particle 1 decays into particles 3 and B. When particle 3 moves in the same direction as particle 2 with a larger velocity so that it can catch up with particle 2, and then particles 2 and 3 collide to form A in the final state. During this process, all intermediate particles are on their mass shell and this process corresponds to the leading Landau singularity.

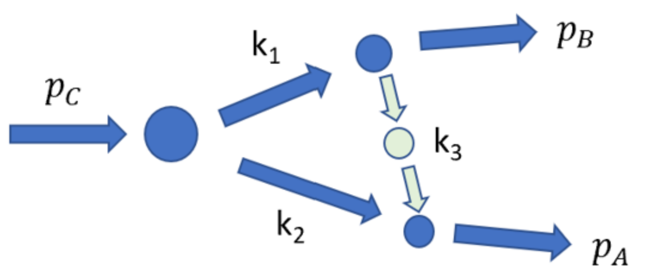

A copious number of physical states, like hadrons, make it easier to satisfy singularity conditions. In this work, we explore several TS scenarios with the kaleidoscopic BSM particle content, such as in supersymmetry models, to discuss the kinematic observables and their physical case. Kinematics at TS derive from Landau Equation’s requirements on momenta. For clarity, Latin subscripts denote the three external momenta p_i as $\{p_A, p_B, p_C\}$. In order for Eq. 2 to have physical solutions, their invariant self-products $\{p_A^2, p_B^2, p_C^2\}$ satisfy the relations

$$\begin{aligned} p_C^2 &\in \left[(m_1+m_2)^2, m_1^2 + m_2^2 + m_2 m_3 + \frac{m_2}{m_3}\left(m_1^2 - p_B^2\right) \right] \\ p_A^2 &\in \left[(m_2+m_3)^2, m_2^2 + m_3^2 + m_1 m_2 + \frac{m_2}{m_1}\left(m_3^2 - p_B^2\right) \right], \end{aligned} \tag{3}$$

where the internal resonant masses need to be positive and at least two internal particles have non-identical values. We consider some typical processes include the Drell-Yan and Vector Boson fusion (VBF) diagrams, as shown below, in which charged BSM particles can occupy the internal line(s) k_i inside the triangle loop.

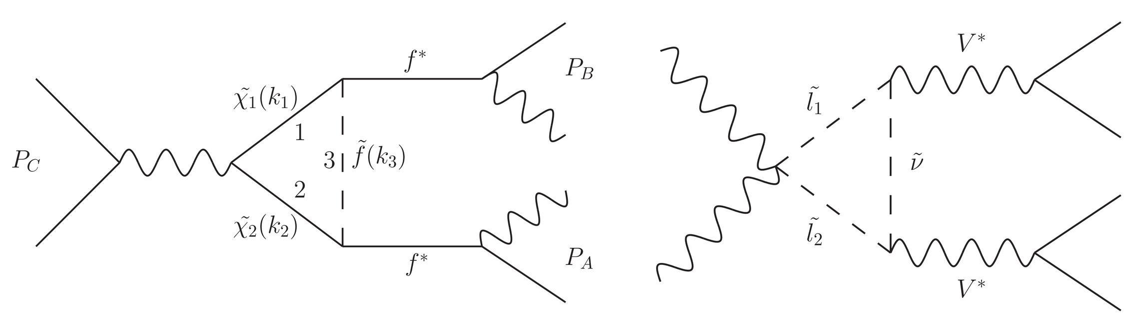

Taking an example with the minimal supersymmetric standard model (MSSM), a Drell-Yan process with fermionic p_A, p_B realizes with neutralino/chargino(s) as k_1, k_2, a sfermion as k_3, and two virtual SM fermions as p_A, p_B. In a VBF process, two initial-state radiated bosons can directly couple to k_1, k_2 with a four-particle vertex, in addition to the diagram of two boson first fusing into an s-channel propagator. Renormalizable four-particle couplings would require BSM bosons as k_i. In the MSSM, possible examples include slepton/squarks completing the triangle loop, e.g. with $\{\tilde{l}, \tilde{l}, \tilde{\nu}\}, \{\tilde{q}, \tilde{q}, \tilde{q}'\}$.

Parameter Space for Triggering TS

Collider reach at TS can cover a large range of BSM particle masses. In terms of m_1 and m_2, their physical solutions satisfies Eq. 2, and for a given collision center-of-mass energy $\sqrt{p_C^2}$ and free m_3, the valid parameter space is shown by the shaded area.

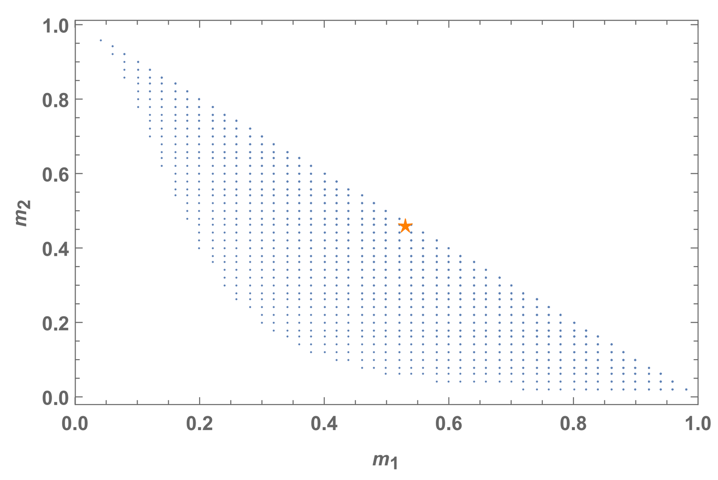

The upper edge of the shaded region, $m_1 + m_2 \leq \sqrt{p_C^2} \leq \sqrt{s}$, corresponds to Eq. 3 lower boundary, and the lower edge corresponds to the Eq. 3 upper boundary. Since the beam particle’s parton distribution allows $\sqrt{p_C^2}$ to be anywhere below the maximal collision energy $\sqrt{s}$, the subspace where m_1, m_2 are too low to hit TS at a given $\sqrt{p_C^2}$ can still trigger TS at a lower value. This allows a high energy collider to sweep through the relevant TS parameter space in an efficient way similar to that for m_1, m_2 pair-production.

The Correlation of External Momentum

It shall be interesting if the TS loop provides extra phenomenon besides conventional BSM pair production, in particular, if the relevant observables are constructed from visible SM final-state particles. So next we will illustrate the relation of internal m_i and external p^2 at TS with given internal BSM masses. Solvable Eq. 2 requires a zero determinant of its β_i’s coefficient matrix:

$$\begin{vmatrix} 1 & y_{12} & y_{13} \\ y_{12} & 1 & y_{23} \\ y_{13} & y_{23} & 1 \end{vmatrix} = 1 + 2 y_{12} y_{23} y_{13} - y_{12}^2 - y_{23}^2 - y_{13}^2 = 0, \tag{4}$$

which contain 6 kinematic parameters. Fixing all three internal BSM masses and one external momentum, The relation between the two remaining external invariant momenta is a Dalitz curve, as shown by the blue solid trajectories in below figure. Its ‘physical’ section satisfies Eq. 2 and is shown in red. Varying the value of the third (fixed) invariant momentum let the physical Dalitz curve sweep across the parameter plane and covers a TS phase space enclosed by the maximal p_A^2 envelope and the minimal p_C^2 from Eq. 3.

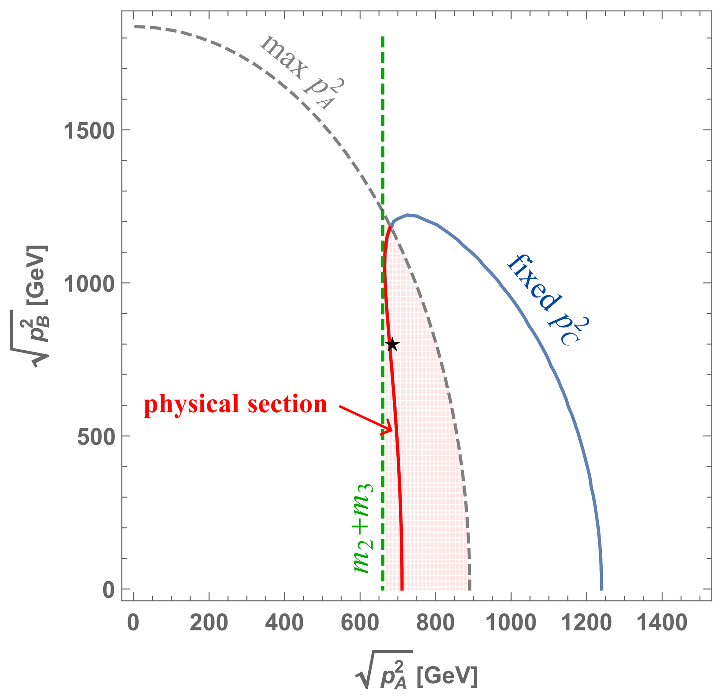

There are two kinds of kinematical features: (i) Peak(s) in distribution in the third invariant momentum when the other two become on-shell. A $\sqrt{s}$ peak emerges if both $\sqrt{p_A^2}, \sqrt{p_B^2}$ identify with physical particles whose masses can locate inside the shaded region in the above figure. (ii) Correlation between two invariant masses when one external momentum is on-shell, i.e. the 2D phase space of the remaining invariant momenta reduces to a Dalitz curve. In practice, the correlation shape will be smeared by both internal/external particle width and detector resolutions, yet it can be looked for with advanced analysis software.

Less Suppressed Scenario

At a large collision energy, $\sqrt{p_A^2}, \sqrt{p_C^2}$ can be much higher than the weak scale. Thus identifying the external line with one (intermediate) single particle can suffer major propagator virtuality suppression $\propto (p_{A,C}^2 - m_{\rm SM}^2)^{-1} \sim p_{A,C}^{-2}$ in the amplitude. However, there are ways to avoid the large virtuality suppression completely in the case of bosons. Some bosonic vertices that carry derivatives (e.g. gauge couplings of bosons) can yield $\partial^\mu \propto p_{A,C}^\mu$. When the propagator further splits to lighter bosons with another derivative coupling, the $k^\mu . k_\mu$ can lift the $p_{A,C}^{-2}$ suppression in the large $p_{A,C}$ limit. A more straight-forward solution is to involve 4-particle gauge-coupling vertices and quartic couplings arising from the scalar potential, which replaces the external momentum with a pair of bosons that can be both put on-shell.

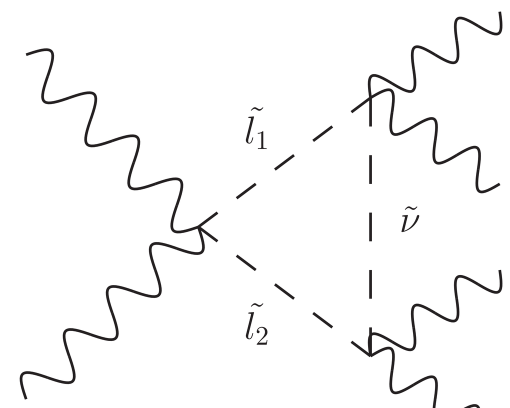

TS features an external momenta dependence in the loop amplitude that becomes singular when Eq. 2 and Eq. 3 are met. When the masses of internal particles and p_B^2, p_C^2 are within the range for the TS to be in the physical region, the enhancement due to TS effects will appear when p_A^2 satisfies the Landau Equation.

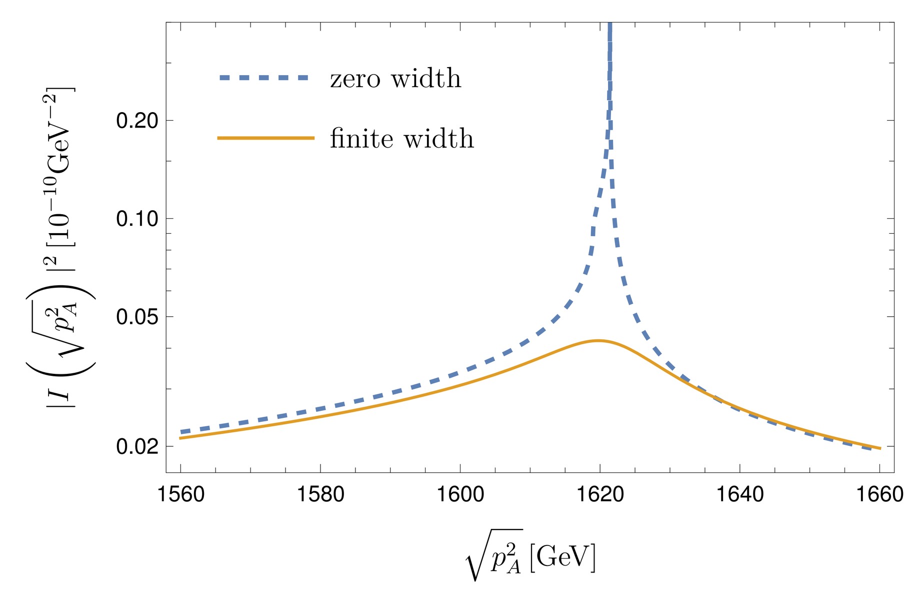

In practice, the internal particles’ width will provide a small imaginary part to the propagators. Therefore the singularity collapses to a finite peak that broadens with the particle widths.

Summary and Discussion

We discussed several specific cases in the MSSM that satisfy TS with Drell-Yan and vector boson fusion processes. The diverse particle spectrum in BSM theories can provide candidate particles to fill in a triangle loop diagram and satisfy triangular singularity at a high energy collider. TS manifestation with BSM loops can lead to a fully identifiable SM final state, offering a unique alternative for new physics. Although TS is still a near-threshold phenomenon, TS can produce a final state purely composed of visible SM particle-systems that carry BSM scale energies. This would help reconstruct and identify these particles at the collider and reveal the so-called compressed BSM particle spectrum.

Angularity in Higgs decay at NNLL′ accuracy

Jiawei Zhu[1,*], Yujin Song[1], Jun Gao[2], Daekyoung Kang[1,**], Tanmay Maji[3]

[1]Key Laboratory of Nuclear Physics and Ion-beam Application (MOE), Fudan University, Shanghai, China 200433

[2]INPAC, Shanghai Key Laboratory for Particle Physics and Cosmology, School of Physics and Astronomy, Shanghai Jiao Tong University, Shanghai 200240, China

[3]Department of Physics, National Institute of Technology, Kurukshetra, Haryana, 136119, India

*jiaweizhu21@m.fudan.edu.cn,**dkang@fudan.edu.cn

Abstract

We present improved theoretical predictions for angularity distribution in Higgs decays into hadrons. Digluon channel is one of main decay channels of Higgs boson decay, and predictions on angularity distribution have large theoretical uncertainty associated with large logarithms. In the framework of SCET, we independently determine the 2-loop constant term in the gluon-jet function of angularity from a fit to NLO QCD results via an asymptotic form with recoil corrections in SCET-II limit and make predictions for resummed angularity distribution at NNLL′ in logarithmic accuracy and $\mathcal{O}(\alpha_s^2)$ in fixed-order accuracy.

1. Motivation

Event shapes are observables designed to characterize the geometric shape of hadron distribution, widely used in study of Higgs hardonic decay and in determination of fundamental parameters in SM. A specific event shape called angularity is defined by:

$$\tau_a = \frac{1}{Q}\sum_i |\mathbf{p}_\perp^i| e^{-|\eta_i|(1-a)} \tag{1}$$

Advantage:

1, Can be used for precision determination of fundamental parameter, e.g. strong coupling constant, Yukawa coupling constant.

2, $a < 2$, reshape the distribution to highlight the physics process we interested.

2. SCET factorization

Soft-collinear effect theory is a theoretical framework for studying the interactions of energetic partons with multiple momentum scales:

$$p_H^\mu \sim Q, \quad p_c^\mu \sim Q\left(\lambda^2, 1, \lambda\right) \quad \text{and} \quad p_s^\mu \sim Q\lambda^{2-a} \tag{2}$$

In Laplace space, Higgs digluon and diquark decay channel can be factorized into:

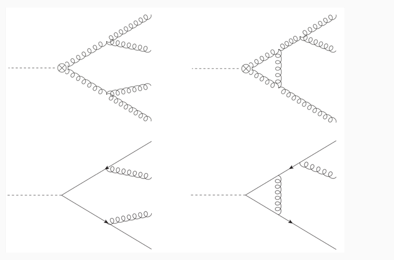

$$\tilde{\Gamma}^i(\nu_a) = \Gamma_B^i(\mu)\, t(m_t^2,\mu)\, H(m_H^2,\mu) \tilde{J}_n^i(\nu_a,\mu)\ \tilde{J}_{\bar{n}}^i(\nu_a,\mu)\ \tilde{S}^i(\nu_a,\mu) \tag{3}$$

$H(m_H^2,\mu)$: hard function, matching from QCD to SCET.

$\tilde{J}_n^i(\nu_a,\mu)$: jet function from collinear radiation.

$\tilde{S}^i(\nu_a,\mu)$: soft function from soft radiation.

Structure of each function at 2-loop:

$$G^i(L_G,\mu_G) = \sum_{n=0}^{\infty}\left(\frac{\alpha_s(\mu_G)}{4\pi}\right)^n G^{i(n)}(L_G)$$

$$G^{i(2)}(L_G) = \left[\frac{1}{2}\left(\Gamma_G^0\right)^2 L_G^4 - \Gamma_G^0\left(\gamma_G^0 + \frac{2}{3}\beta_0\right)L_G^3 + \left(\Gamma_G^1 + \frac{1}{2}\left(\gamma_G^0\right)^2 + \gamma_G^0\beta_0 + c^1\Gamma_G^0\right)L_G^2 - \left(\gamma_G^1 + c^1\gamma_G^0 + 2c^1\beta_0\right)L_G + \mathbf{c^2}\right] \tag{4}$$

All functions are known up to 2-loop except for the 2-loop constant in gluon-jet function, $\mathbf{c_g^2}$.

3. Determination strategy

Full QCD gives:

$$\frac{1}{\Gamma_0}\frac{d\Gamma}{d\tau_a} = A\delta(\tau_a) + [B(\tau_a)]_+ + r(\tau_a) \tag{5}$$

SCET gives:

$$\frac{1}{\Gamma_0}\frac{d\Gamma_s}{d\tau_a} = A\delta(\tau_a) + [B(\tau_a)]_+ \tag{6}$$

Total decay rate gives:

$$\frac{\Gamma_t}{\Gamma_0} = \int_0^1 d\tau_a' \frac{1}{\Gamma_0}\frac{d\Gamma}{d\tau_a'} = A + r_c \tag{7}$$

where $\mathbf{c^2}$ in each function contributes to A, while A in Eq. (5) from MC is not captured, in Eq. (6) lacks $\mathbf{c_g^2}$ in gluon-jet function, and in Eq. (7) cannot picked up.

Strategy:

Step 1, Obtain $r(\tau_a)$ by subtracting SCET singular distribution Eq. (6) from MC full QCD distribution Eq. (5), and integrate out τ_a from $\tau_a^{\min}$ to $\tau_a^{\max}$ to get remainder function.

Step 2, Fit remainder function to get asymptotic result r_c in $\tau_a \to 0$.

Step 3, Subtract r_c in total decay rate Eq. (7), and obtain unknown $\mathbf{c_g^2}$ in gluon-jet function in A.

Challenge:

1, Due to finite machine precision, $r(\tau_a)$ from MC has large uncertainty.

2, Convergent of r_c becomes slow in lage a due to recoil correction.

Our Solution: Asymptotic approach with recoil correction under Tikhonov regularization.

Asymptotic behaviour of $r(\tau_a)$ in $a \le 0$:

$$\sum_{i=0}^{3} \alpha_i \ln^i \tau_a \quad \text{at NLO} \tag{8}$$

Recoil correction at $0 < a < 1$ is from $p_n^\perp \sim p_s^\perp$:

$$\sum_{n=1}^{\lceil 1/(1-a)) \rceil - 1} \frac{e_{n,2}\ln^2\tau_a + e_{n,1}\ln\tau_a + e_{n,0}}{\tau_a^{1-n(1-a)}} \quad \text{at NLO (assumption)} \tag{9}$$

which based on convolution of 1-loop recoil correction in soft function and 1-loop jet function.

4. Examination and determination

Examination: Known c_q^2 in quark-jet function in Higgs diquark decay channel:

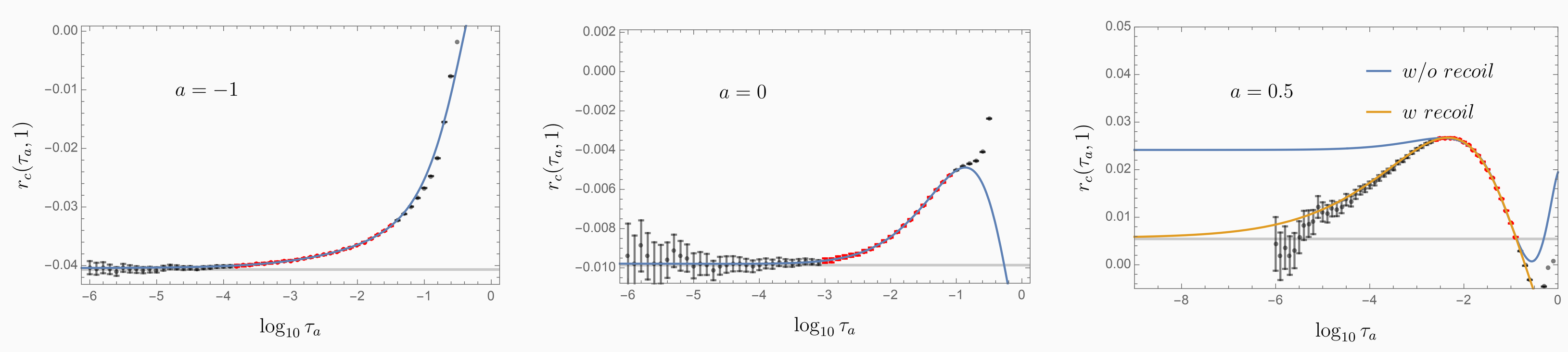

Red (Black) error bar: the data in (out of) fitting region.

Gray line: known result.

Determination: $\mathbf{c_g^2}$ in gluon-jet function in Higgs digluon decay channel:

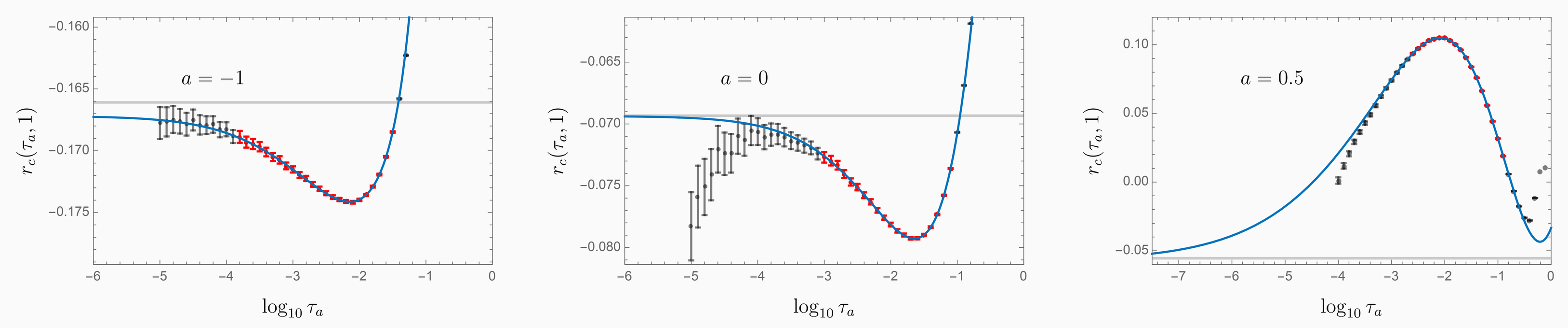

Gray line: known result (unpublished thesis, number read from plot).

5. Resummation

Hard, jet and soft function are RG evolved from its nature scale μ_G to a target scale μ, shown in below equation and left plot. Profile function $\mu^i(\tau_a)$ and uncertainty estimation are shown in below right plot, where profile is designed to connect resummation region and fixed-order region, and uncertainty estimation is band method.

$$G(\nu,\mu) = G(\nu,\mu_G)e^{K_G(\mu_G,\mu)+j_G\eta_G(\mu_G,\mu)L_G} \tag{10}$$

$$\text{where } e^{K_G(\mu_G,\mu)+j_G\eta_G(\mu_G,\mu)L_G} = \underbrace{\sum (\alpha_s L)^n L}_{\text{LL}} + \underbrace{\sum (\alpha_s L)^n}_{\text{NLL}} + \cdots$$

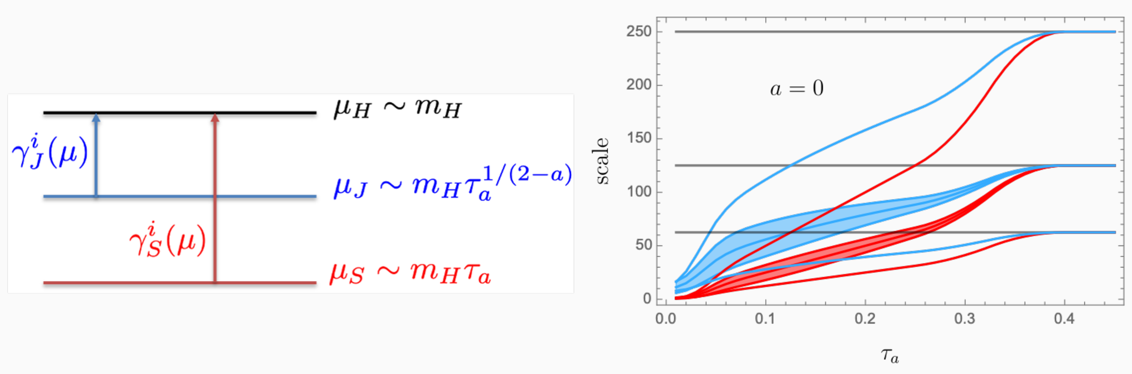

Prediction of resummed angularity distribution of Higgs digluon decay channel:

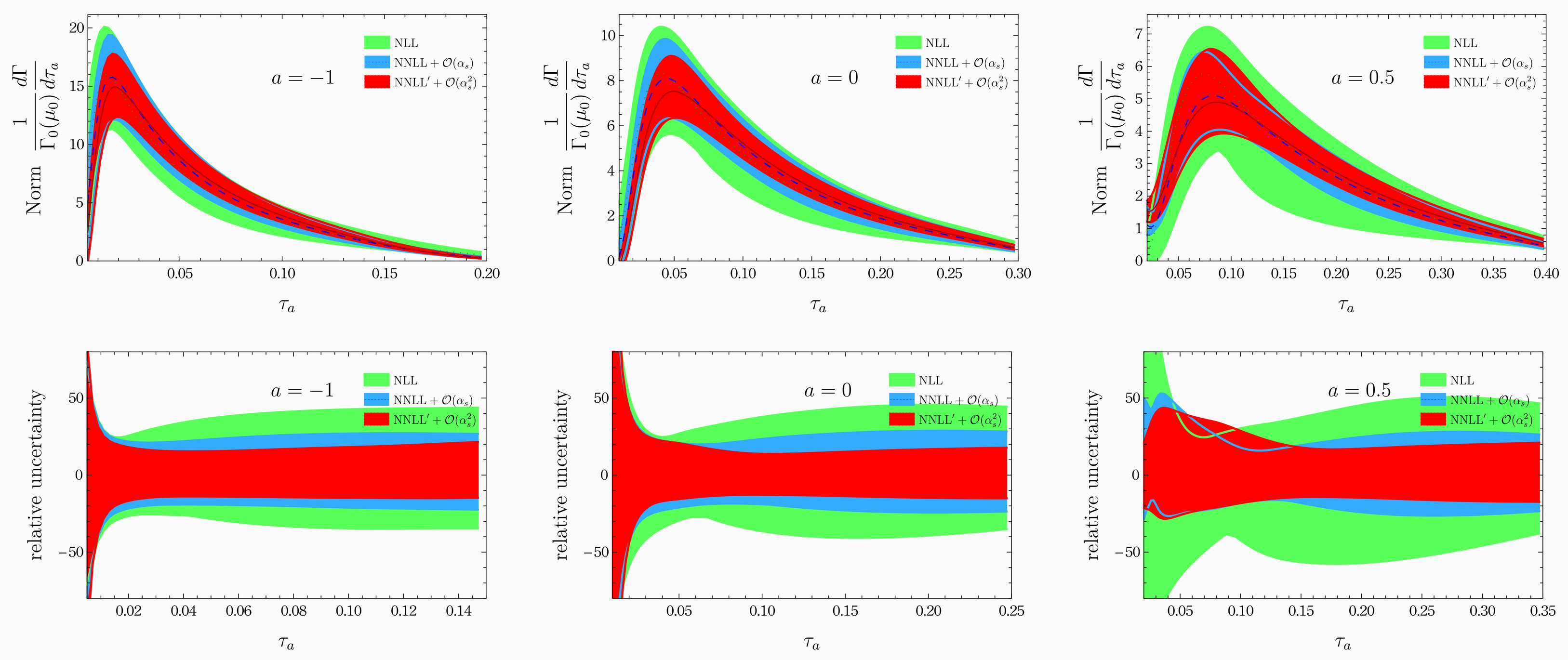

References

[1] Guido Bell et al. "e^+e^- angularity distributions at NNLL′ accuracy". In: JHEP 01 (2019), p. 147. DOI: 10.1007/JHEP01(2019)147. arXiv: 1808.07867 [hep-ph].

[2] Jun Gao et al. "Thrust distribution in Higgs decays at the next-to-leading order and beyond". In: JHEP 03 (2019), p. 030. DOI: 10.1007/JHEP03(2019)030. arXiv: 1901.02253 [hep-ph].

[3] Ankita Budhraja, Ambar Jain, and Massimiliano Procura. "One-loop angularity distributions with recoil using Soft-Collinear Effective Theory". In: JHEP 08 (2019), p. 144. DOI: 10.1007/JHEP08(2019)144. arXiv: 1903.11087 [hep-ph].

Reconstruction Algorithm of Cluster Counting in Drift Chambers

Shuaiyi Liu[1], Guang Zhao[1], Zhefei Tian[2], Brunella D'Anzi[4], Mingyi Dong[1], Nicola De Filippis[4], Xu Gao[3], Francesco Grancagnolo[4], Fei Huang[1], Shengjie Jin[1], Gang Li[1], Linghui Wu[1], Zhenyu Zhang[2]
[1]Institute of High Energy Physics, Chinese Academy of Science, China
[2]Wuhan University, China
[3]Jilin University, China
[4]Instituto Nazionale di Fisica Nucleare, Italy

Introduction

Drift Chamber in CEPC 4th conceptual detector

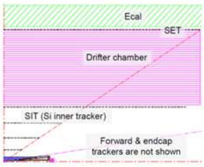

- Tracker with silicon tracker and a drift chamber
- The chamber optimized for PID with cluster counting technique
- Up to 20GeV/c K/π separation power better than 2σ required
- Benefited momentum resolution at low momentum

Preliminary DC parameters	
Inner radius	800mm
Outer radius	1800mm
Cell size	18 mm×18 mm
Gas mixture	He/iC_4H_{10}=90:10
Length of outermost wires (cosθ=0.82)	5143mm

dE/dx vs dN/dx measurement

dN/dx
- Number of primary ionization clusters per unit length
- Poisson distribution
- Small fluctuation

dE/dx
- Energy loss per unit length
- Landau distribution
- Large fluctuation

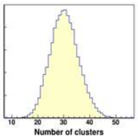

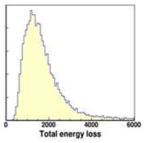

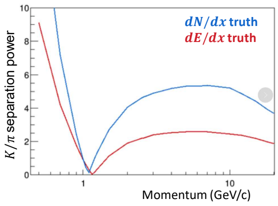

dN/dx has a much better K/π separation power up to 20 GeV/c compared to dE/dx (MC truth)

Advantages of Particle identification

- Reduce combination background
- Improve mass resolution
- Improve jet energy resolution
- Benefit flavor tagging

Simulation of $B^0/B_s^0 \to \pi^+\pi^-$ with Delphes

Without PID

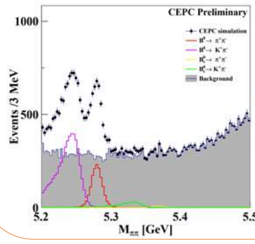

With PID

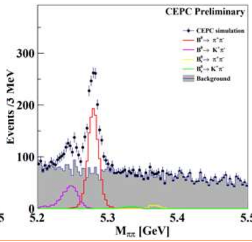

Algorithm for Simulated Samples

Reconstruction of cluster counting

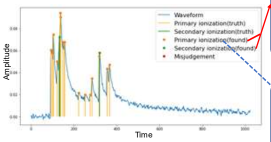

Step1. Peak Finding
Discriminate peaks (both primary and secondary) except from the noises (classification problem)

Step2. Clusterization:
Determine the number of clusters (N_{cls}) from the detected peaks (regression problem)

Reconstruction algorithms

- **Classical method**(developed)
  - Derivative-based peak finding + clusterization with peak merge
- **Deep learning based algorithm** (ongoing)
  - Peak finding with LSTM + clusterization with DGCNN

Preliminary results with classical algorithm

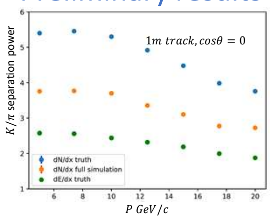

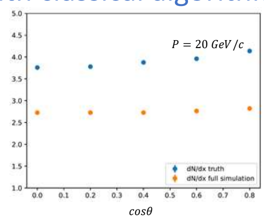

K/π separation power is better than 2 sigma at 20GeV/c in dN/dx full simulation

Deep learning based algorithm

Peak finding with LSTM (Long Short Term Memory)

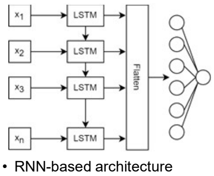

- RNN-based architecture
- Binary classification of signals and noises on slide windows of peak candidates

Clusterization with DGCNN (Dynamic Graphic Convolutional Neural Network)

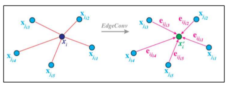

arXiv: 1801.07829

- GNN-based architecture
- Massage passing through neighbor nodes ⟺ Clusterization of electron timings from the same primary cluster
- Binary classification of primary and secondary electrons

Comparison between Classical & Deep learning algorithms

Peak finding

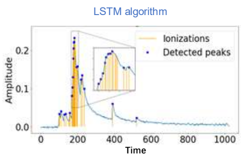

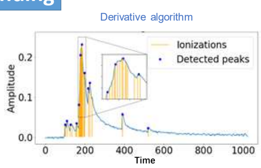

LSTM algorithm is more efficient for pile-up detection

Clusterization

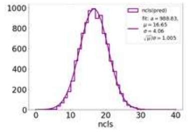

Deep learning algorithm closer to MC truth

Clusterization Method	μ	σ	σ/μ
MC truth	16.53	3.93	23.8%
Classical algorithm	18.67	4.60	24.6%
Deep learning	16.65	4.06	24.4%

Algorithm of Test Beam Samples

Deep learning algorithm in beam test data analysis

Beam Test for DC prototype

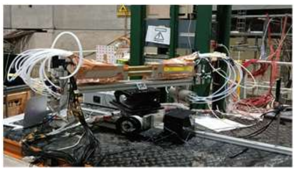

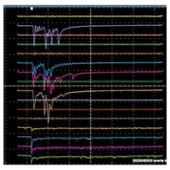

Difficulties for ML in data samples

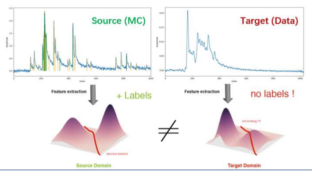

- Domain shift between MC/data
- Lack of labels in data

→ Semi-supervised DeepJDOT

Deep Joint Distribution Optimal Transport (DeepJDOT)

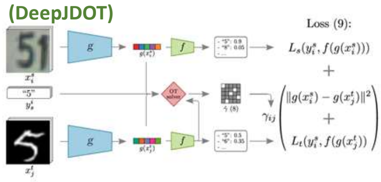

- Original DeepJDOT (arxiv:1803.10081)
- We develop the semi-supervised version of DeepJDOT

Validation on MC experiment

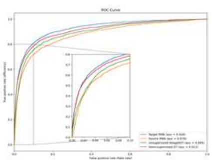

Model	AUC	pAUC (FPR<0.1)
Ideal model*	0.926	0.812
Source RNN	0.878	0.749
Unsupervised DeepJDOT	0.895	0.769
Semi-supervised DeepJDOT	0.912	0.793

* Supervised model assuming there are labels in the training sample

Details of beam test in Guang's talk "**Drift chamber with cluster counting techniques for CEPC**" at "**PID and other detectors:3** " session.

Preliminary results of peak finding

Comparison between classical and ML peak finding algorithms

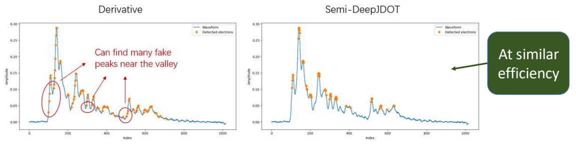

Deep learning has better performance on finding peaks reasonably on data.

Number of Peaks distributions of data with different angles

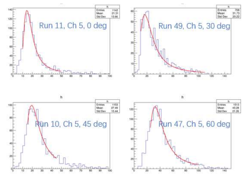

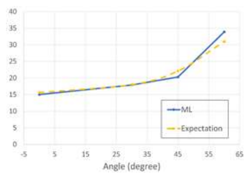

The result of deep learning algorithm has consistent tendency with theoretical expectation.

Contact: Shuaiyi Liu e-mail: liusy@ihep.ac.cn
The 2023 International Workshop on the High Energy Circular Electron Positron Collider, 2023 10.23-27, Nanjing

Institute of High Energy Physics
Chinese Academy of Sciences

HEP@home : A Volunteer Computing Project to Run Fast Simulation with Delphes for CEPC

Ran Du, Jingyan Shi, Gang Li
{duran, shijy, li.gang}@ihep.ac.cn
Institute of High Energy Physics ,Chinese Academy of Sciences, Beijing, China, 100049

1 Introduction

Delphes is a C++ framework to perform a fast multipurpose detector response simulation. The Circular Electron Positron Collider (CEPC) experiment runs fast simulation with a modified Delphes based on specific scientific objectives. To get more computing resources for CEPC and make CEPC better known by public, a Volunteer Computing project based on BOINC, HEP@home, is developed to run Delphes as its first application.
The architecture of the HEP@home project is shown in Figure 1. Five parts are developed including CEPC Delphes App, work generator, validator, assimilator and project web site.

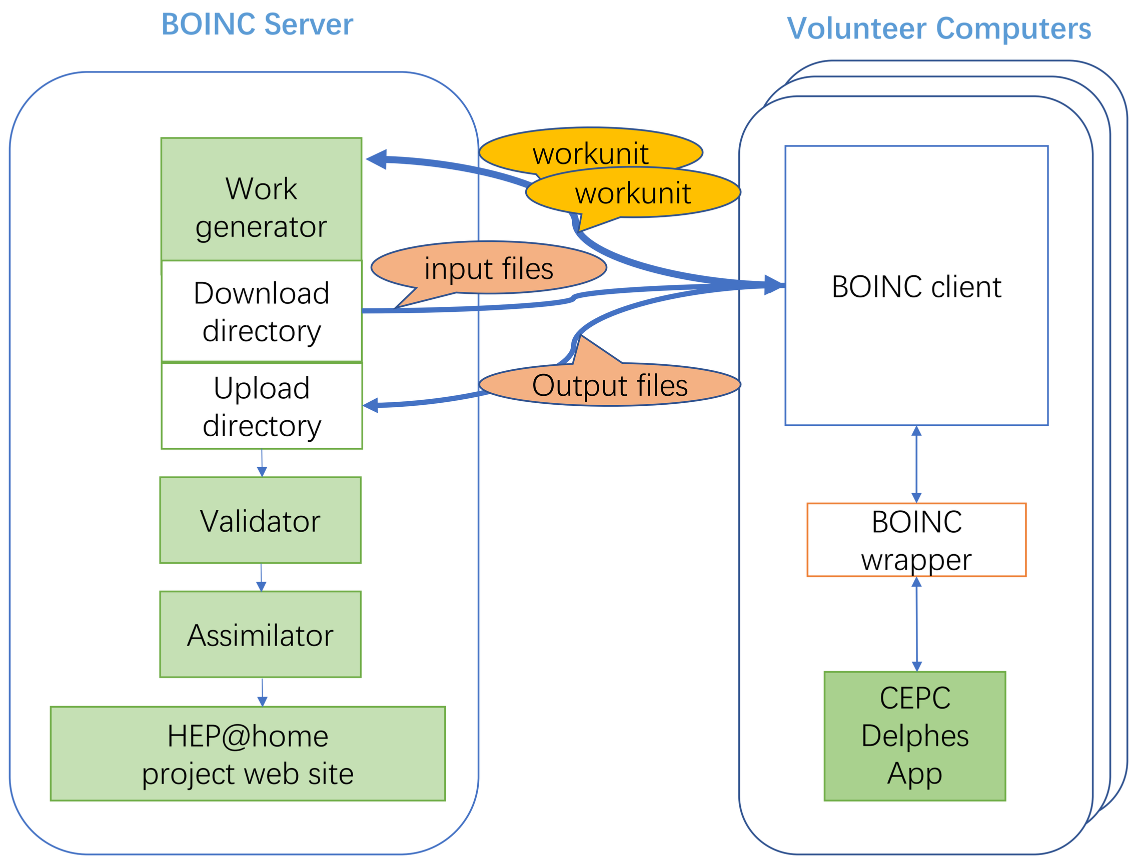

Figure 1: Architecture of the HEP@home project.

2 CEPC Delphes App

Delphes is a High Throughput Computing (HTC) application with small input and output files. Besides, to compile and run Delphes, only ROOT software is dependent, which makes it appropriate to run as a Volunteer Computing application.
To run CEPC Delphes on Windows, a customized docker image is composed. This image contains all dependent software to run Delphes. Besides, to get high availability, this image is uploaded to three docker registries. Figure 2 shows the image uploaded to dockerhub.

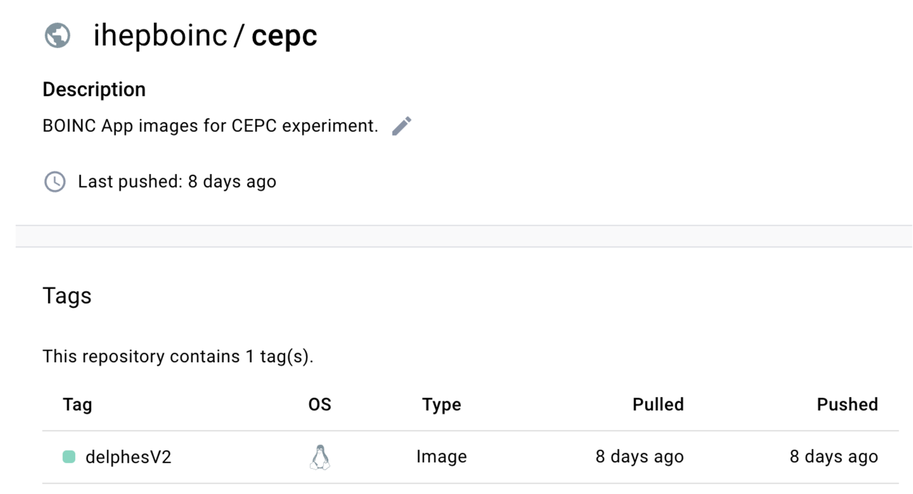

Figure 2: Dockerhub image of the CEPC Delphes App to run on volunteer computers.

3 Work Generator

The work generator is developed to submit workunits(jobs) in batches. To make submission in order, a MariaDB database delphes_task_db is designed and adopted. All the metadata of stdhep input files are organized into a three-level hierarchy consisted with tasks, subtasks and input files.
Besides, to make sure the server load is under control, submitted workunits will be hold and saved into a buffer if the server load is heavier than threshold. When the load dropped back to a normal level, buffered workunits will be resubmitted. Figure 3 shows the components of the work generator.

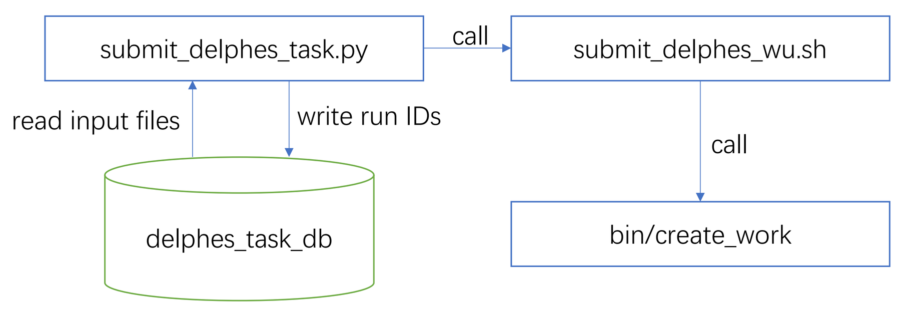

Figure 3: Components of the work generator.

4 Validator

Each output root file generated by Delphes on volunteer computers will be uploaded back to the server. When the output files are uploaded, the validator will be called to double check based on the requirements of application, and the volunteers will get a number of credits if output files are valid.
Different applications have specific validation metrics, in our case, the validation metrics are number of events, number of particles, momentum resolution and energy resolution. Figure 4 show the components of the validator for Delphes application.

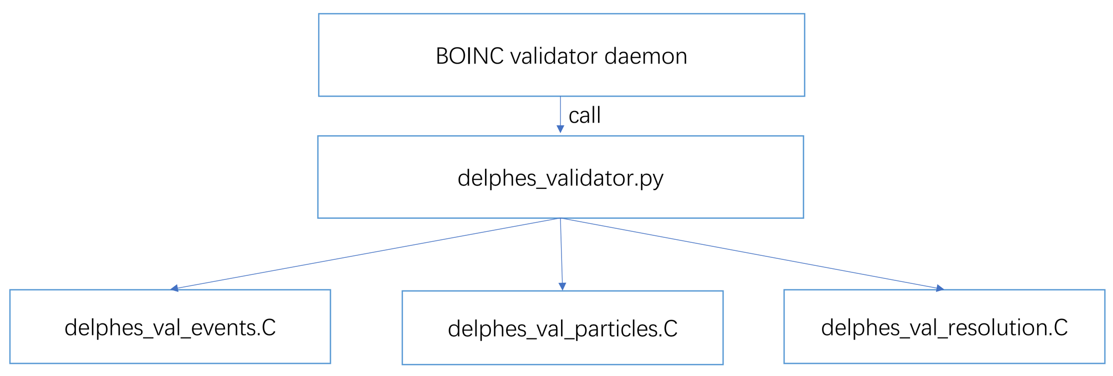

Figure 4: Components of the validator.

5 Assimilator

Valid output files will be handled by the assimilator. The assimilator for the Delphes application will save root files and image files in Lustre file system and a database named hep_assimi_db. The root files saved in the Lustre File System can be accessed by physicists for later use, and meta data of these foot files are saved in hep_assimi_db. Meanwhile, image files saved in hep_assimi_db will be displayed on the project web site. Figure 5 shows the components of the assimilator.

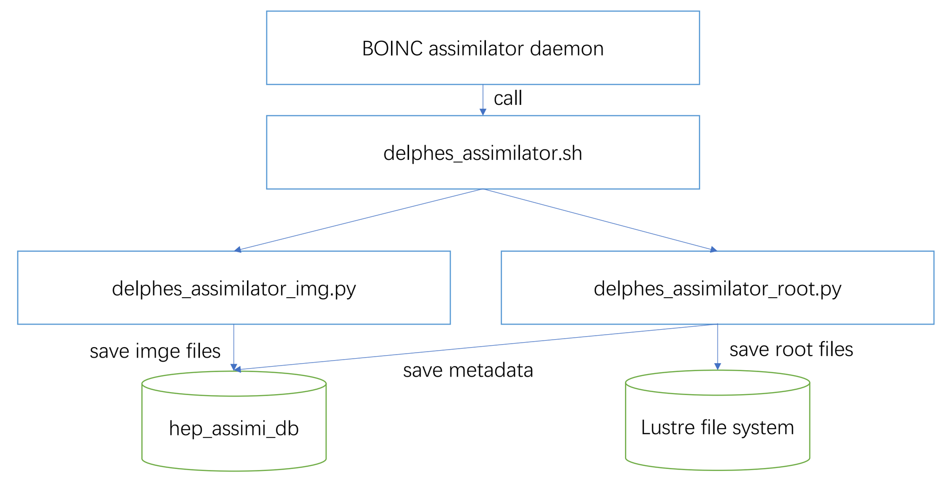

Figure 5: Components of the assimilator.

6 Join HEP@home Project

As we mentioned earlier, image files generated by the assimilator will be displayed on the project web site as shown in Figure 6(a). Figure 6(b) shows the procedure of running Delphes on a volunteer computer. Because the requirements of CEPC computing resources are quite large, we expect more and more volunteers and computers will join us. Scan the QR code and visit HEP@home website, You are warmly welcomed to join us by scanning the QR code.

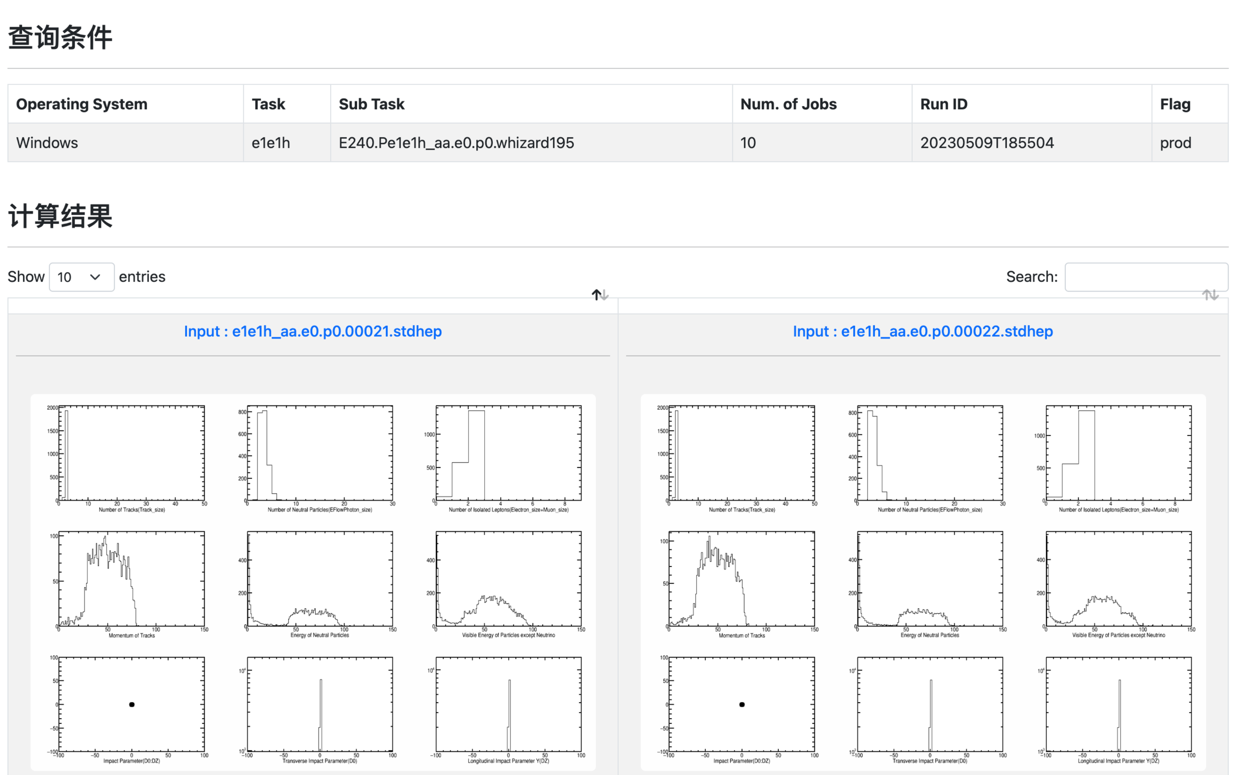

(a)

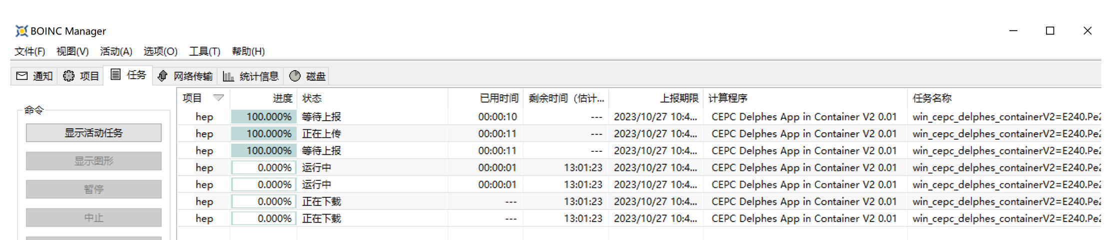

(b)

Join HEP@home
https://ihepboinc.ihep.ac.cn/hep

(c)

Figure 6: (a)Output images of Delphes application. (b)Delphes workunits run on a volunteer computers. (c)QR code of HEP@home project.

Neural network algorithm for HL-LHC ATLAS hardware τ trigger

Yuval Frid, Maayan Tamari, Boping Chen, Liron Barak
Tel Aviv University
boping.chen@cern.ch

1. Introduction

- The High-Luminosity Large Hadron Collider (HL-LHC) is planned to start to collect data in 2029 and achieve 4000 fb^{-1} at ATLAS detector, with an upgraded new global trigger subsystem to be added into the hardware trigger.
- Due to the much higher pile-up condition, the performance of the current hardware trigger algorithm will be largely degraded, especially for the low energy region.

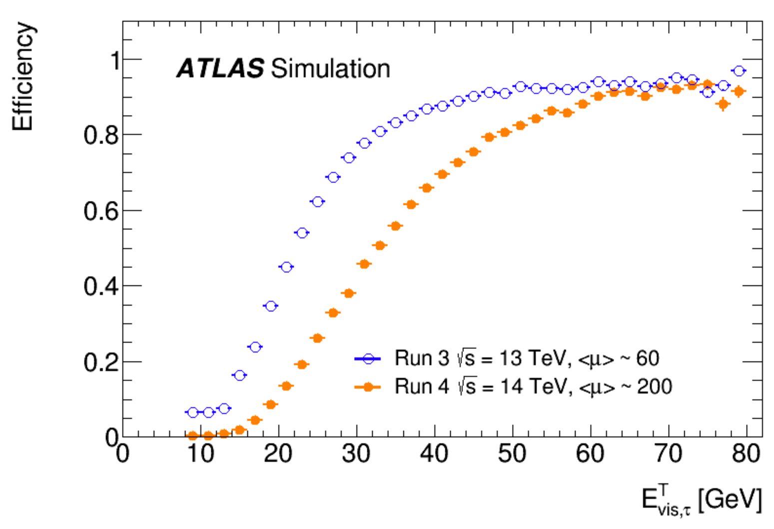

Figure 1: Current τ trigger performance with Run 3 sample (blue) and Run 4 (HL-LHC) sample (orange)

- Since more advanced Field Programmable Gate Arrays (FPGAs) will be implemented, it is possible to run machine learning and even neural networks (NN) at the hardware trigger level.
- Several NN structures, including CNN/DNN, are tested, and the software high level synthesis for machine learning (HLS4ML) is used to create firmware implementation of the NN.
- Compared with the current ATLAS default τ trigger algorithm, the NN can significantly improve the performance of the low energy regime.

2. NN input and structure

- Signal: Standard Model $Z \to \tau\tau$. Background: QCD dijet events.
- Using cell information from EM and Had Calorimeter.
- Seeding with local maximum from upstream, using all the cells within 0.3 x 0.3 in $\eta \times \phi$ around the seed to build the input.
- Different calorimeter layers have different granularity. Rebin or split the cell to get the same granularity for all the layers.

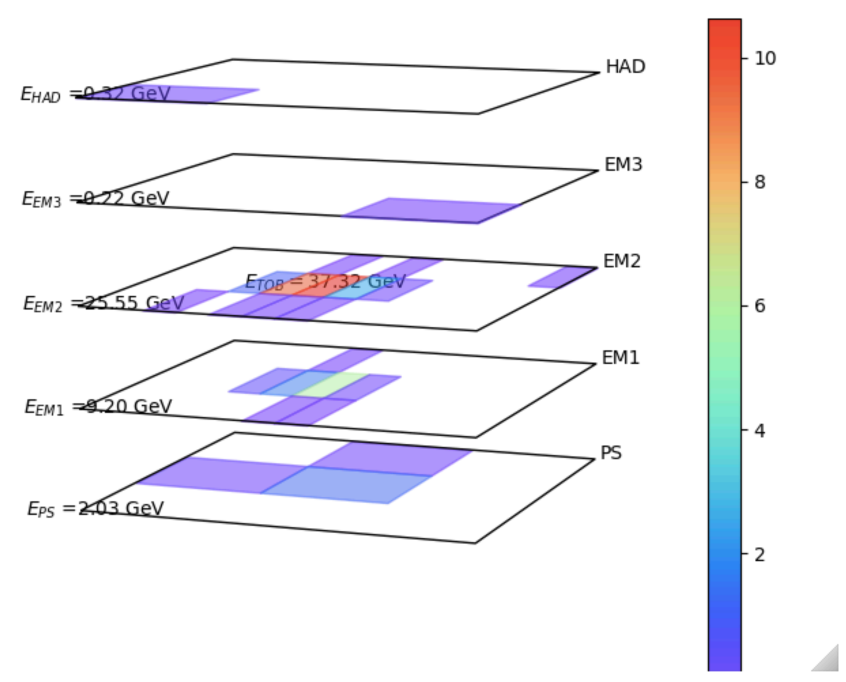

Figure 2: Example of signal input

- Convolutional neural network (CNN) is used for the NN study as a common image identification method.
- The input is treated as a 3x12 image with 5 channels.
- CNN consists of three 2D convolutional layers with kernel size 3x3, two 2D MaxPool layers, and one linear layer to flatten the tensor to a single score.
- Output is one single score between 1 (as signal) and 0 (as background).
- The CNN consists of 7 layers with 12821 parameters
- The threshold is calculated to achieve the background fake rate for the di-τ trigger.

3. NN performance

- Figure below shows signal efficiency vs transverse energy of visible τ.
- Orange is for the current ATLAS default τ trigger (Run 3) algorithm. Blue is the using the CNN score. Green is the using the CNN score multiplied by the total transverse energy of the input image.
- The raw CNN performance (blue) is much better than the current Run 3 algorithm in the low energy region, but worse in the high energy region. After reweighting with the transverse energy (green), the reweighted CNN performance is better than the Run 3 algorithm for the whole range.

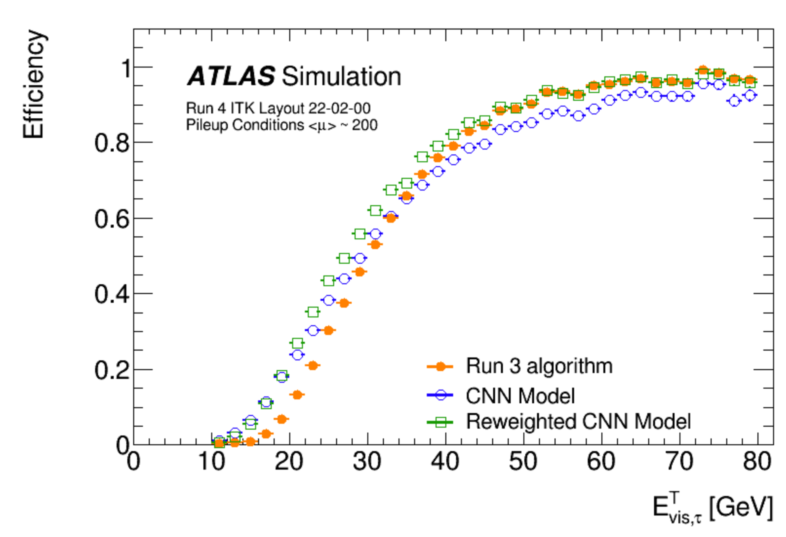

Figure 3: Example of signal input

4. HLS4ML and performance

- HLS4ML is a Python package for machine learning inference in FPGAs.
- It can be used to create firmware implementations of machine learning algorithms using high level synthesis language (HLS), by translating traditional open-source machine learning package models into HLS for microsecond-scale latency on predictions.
- It supports different models, including DNN, RNN and CNN.

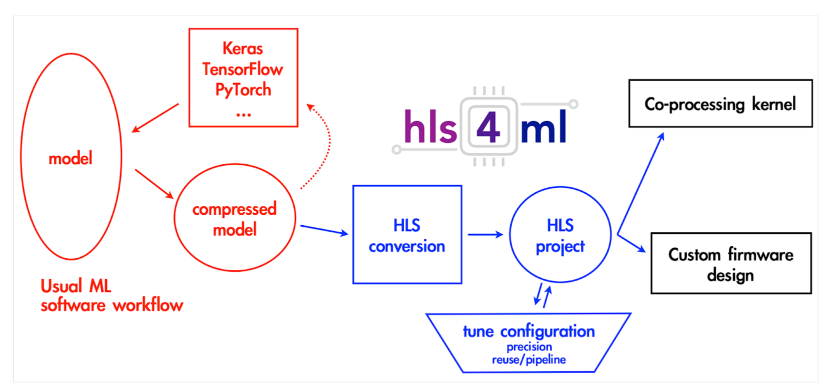

Figure 4: Example of signal input

- Implementation is done on the xcvu9P FPGA.
- For the latency strategy: 1.05% FF, 4.95% LUT, and 32.82% DSP slices, with an estimated latency of 104 clock cycles (520 ns).
- For the resources strategy: 0.52% FF, 1.61% LUT, and 20.82% DSP slices, with an estimated latency of 548-561 clock cycles (2.7 ms).

5. Summary

- The ALTAS trigger system will be upgraded for the HL-LHC, with a new trigger system and more advanced FPGAs.
- Current τ trigger algorithm will be largely degraded due to the much higher pile-up condition for the HL-LHC.
- It is possible to implement the NN to have a better trigger performance.

References

[1] FastML Team. fastmachinelearning/hls4ml, 2023.
[2] Yuval Frid. Neural Network Algorithms For HL-LHC Tau Trigger In ATLAS, 2021.